Electronic Supplementary Information

Ruthenium confined within hollow spherical carbon nitride as an efficient catalyst for triggering peroxymonosulfate

Yu Yin,[a, b] Shuoyuan Tian,[c] Bing Hu,[c] Abdul Hannan Asif,[d] Sheng Cui,[a, b, *] Shaobin Wang,[e] Hongqi Sun,[d, *]

[a] College of Materials Science and Engineering, State Key Laboratory of Materials-Oriented Chemical Engineering, Nanjing Tech University, Nanjing 211816, China

[b] Jiangsu Collaborative Innovation Center for Advanced Inorganic Function Composites, Nanjing Tech University, Nanjing 211816, China

[c] School of Environmental and Chemical Engineering, Jiangsu University of Science and Technology, Zhenjiang 212100, China

[d] School of Molecular Sciences, The University of Western Australia, 35 Stirling Highway, Crawley, WA 6009, Australia

[e] School of Chemical Engineering, The University of Adelaide, Adelaide, SA 5005, Australia

[*] Corresponding authors.

E-mail: scui@njtech.edu.cn (S. Cui), hongqi.sun@uwa.edu.au (H. Sun).

Text S1. Chemicals and Reagents

The water mentioned in this contribution was deionized water. Ruthenium trichloride ($RuCl_3$, 99%) and 5,5-dimethyl-1-pyrroline (DMPO, $C_6H_{11}NO$, 97%) were purchased from Aladdin Co., Ltd. Melamine ($C_3H_6N_6$, 99%), cyanuric acid ($C_3H_3N_3O_3$, 98%), acetaminophen (ACT, $C_8H_9NO_2$, 98%), 2,2,6,6-tetramethylpiperidine (TEMP, $C_9H_{19}N$, 98%), 1,4-benzoquinone, (p-BQ, $C_6H_4O_2$, 98%) and L-histidine ($C_6H_9N_3O_2$, 99%) were obtained from Energy Chemical Reagent Co., Ltd. Sodium chloride (NaCl, 99.5%), sodium nitrate ($NaNO_3$, 99.5%), sodium bicarbonate ($NaHCO_3$, 99.5%), sodium sulfate (Na_2SO_4, 99.5%), potassium sulfate (K_2SO_4, 99%), magnesium sulfate ($MgSO_4$, 99%), calcium sulfate ($CaSO_4$, 98%), methanol (MeOH, CH_4O 99.8%), ethanol absolute (EtOH, C_2H_6O, 99.7%), tert-butanol (TBA, $C_4H_{10}O$, 99.5%), dimethyl sulfoxide (DMSO, C_2H_6OS, 99.5%), sulfuric acid (H_2SO_4, 95%) and potassium hydroxide (KOH, 90%) were obtained from Sinopharm Chemical Reagent Co., Ltd. Peroxymonosulfate (PMS, $KHSO_5{\cdot}0.5KHSO_4{\cdot}0.5K_2SO_4$, 99%) was acquired from Sigma Aldrich. All the chemicals were of the analytical grade and used directly without further purification.

Text S2. Characterization

The morphology of *hs*CN and its Ru containing samples was characterized by field emission scanning electron microscope (FESEM, Quanta FEG 250). High resolution transmission electron microscopy (HRTEM) images were obtained from FEI Tecnai G2 F20. For HRTEM analysis, samples were ultrasonic dispersed in ethanol, impregnated with carbon film coated copper mesh and dried. Under the irradiation of Cu Kα X-ray at 40 kV and 30 mA, the X-ray powder diffraction (XRD) patterns in the range of 5~80° were recorded with the Japanese Shimazu XRD-6100 diffractometer at the scanning speed of 8^o min^{-1} (wide-angle diffraction). The electronic structure and elemental composition of the catalyst were determined by X-ray photoelectron spectroscopy (XPS) on the AXIS-ULTRA DLD instrument at Shimadzu, Japan, and the binding energy was calibrated by C1s peak at 284.6eV. An inductively coupled plasma optical emission spectrometer (ICP-OES, PerkinElmer, Avio 200) was applied to measure the content of Ru in the catalyst and the dissolution contents of Ru metal during the reaction. The adsorption isotherms of N_2 were measured on Belsorp-max at -196 ^{o}C, and the samples were degassed at 200 ^{o}C for 4 h prior to testing. The

specific surface area of the samples was also obtained by Brunauer-Emmett-Teller (BET) method.

Bruker's electron paramagnetic resonance spectrometer (EPR, EMX Plus) was used to detect active free radicals produced in advanced oxidation reactions. First, 20 mg L^{-1} ACT solution, 0.2 g L^{-1} 0.34Ru-*hs*CN suspension and 0.2 g L^{-1} PMS solution were prepared respectively. Then 200 μL of the configured ACT solution, 200 μL of 0.34Ru-*hs*CN solution, and 20 μL of DMPO were mixed to capture $SO_4^{\bullet -}$ and $^{\bullet}OH$. Finally, 200 μL PMS solution was added to initiate the reaction, and the reaction solution was taken out at fixed intervals (1, 5, 10 min) for EPR tests. Similarly, 20 μL TEMP is used instead of DMPO to capture $^1O_2$. In addition, water was replaced by MeOH to capture $O_2^{\bullet -}$ by DMPO. Agilent 6110 liquid chromatography - mass spectrometry (LC-MS) was used to determine the intermediates of ACT removal in Ru-*hs*CN/PMS system.

Text S3. Reaction between PMS and L-histidine

The reaction between PMS and L-histidine was conducted at 25 ℃. 5 mM of L-histidine was added into 250 mL of PMS solution (2.0 g·L^{-1}) with thoroughly stirring. At a specific time interval, 0.1 mL of reaction solution was withdrawn and filtered through a 0.22 μm filter membrane for further measurement. For measuring the concentration of PMS, 4.0 g of KI and 0.2 g of $NaHCO_3$ were added into 40 mL of water and thoroughly dissolved. 0.1 mL of reaction solution was extracted and added into 4 mL of above solution. The concentration of PMS was then tested on an ultraviolet-visible spectrophotometer Shimadzu UV-2550 at the absorbance wavelength of 352 nm.

Text S4. Contribution of $^1O_2$

The contribution of $^1O_2$ to ACT degradation was calculated by Eq. S1, where k_0 represents the reaction rate constant without quencher, k_1 represents the rate constant after adding sufficient quencher of L-histidine during the reaction.

$$\lambda[^1O_2] = (k_0 - k_1)/k_0 \qquad \text{（Eq. S1）}$$

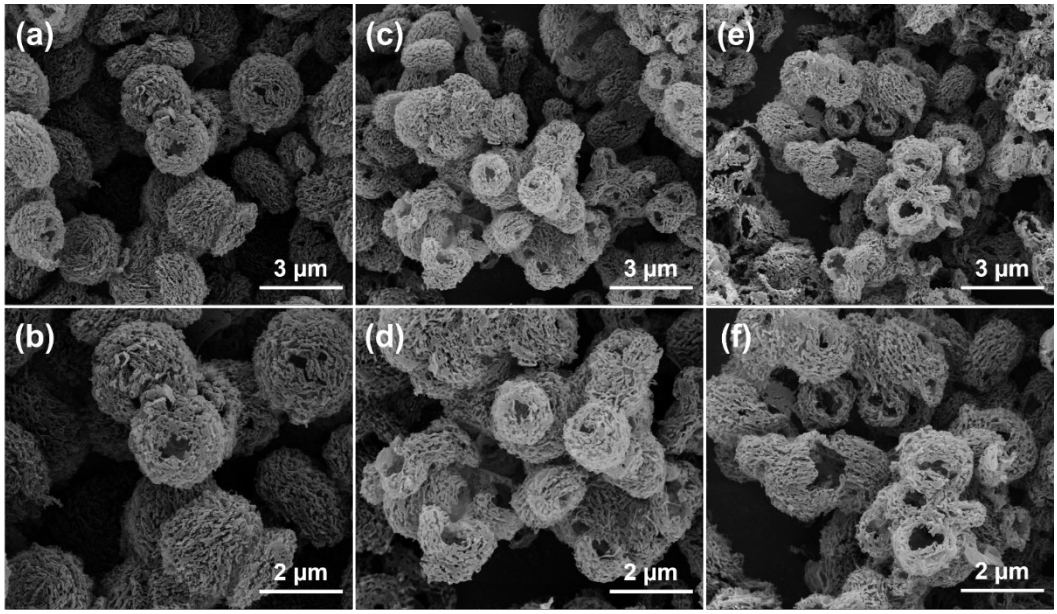

Figure S1. SEM images of (a-b) 0.08Ru-*hs*CN; (c-d) 0.14Ru-*hs*CN and (e-f) 0.46Ru-*hs*CN.

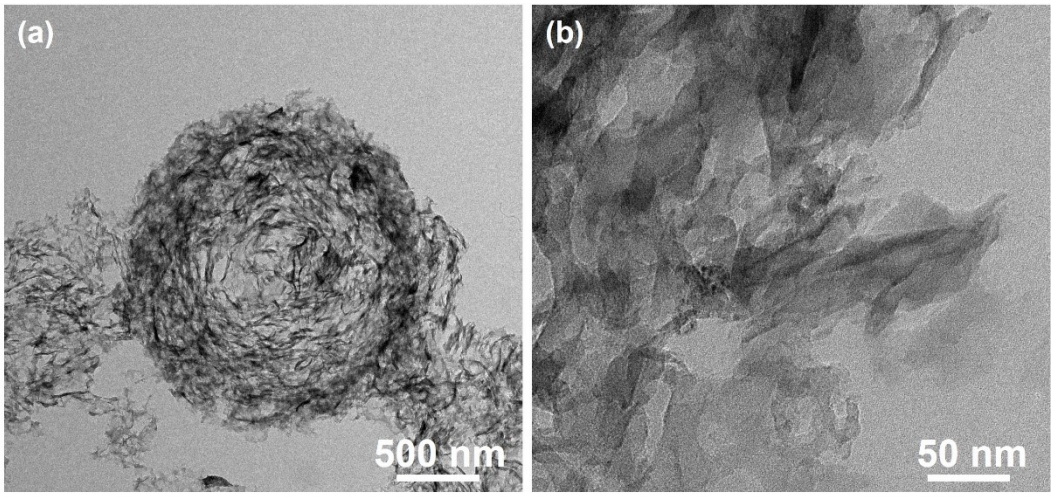

Figure S2. HRTEM images of 0.34Ru-*hs*CN-*imp*.

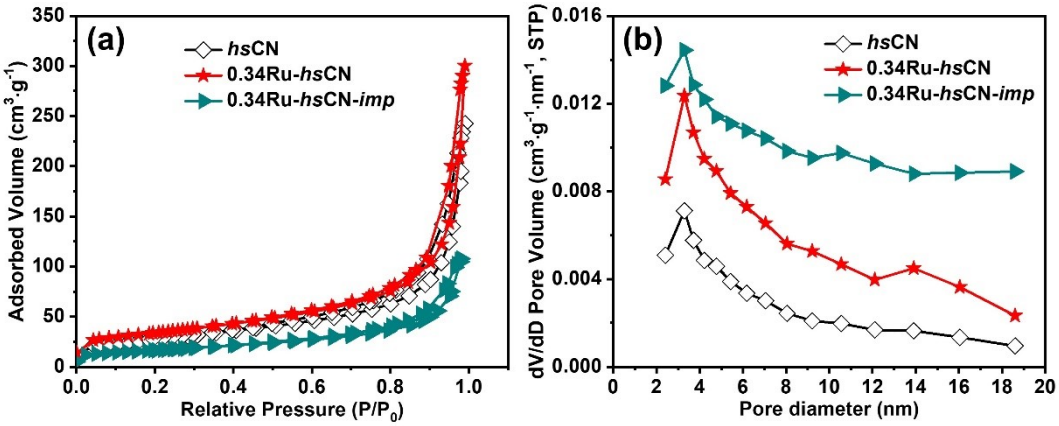

Figure S3. (a) N_2 adsorption-desorption isotherms and (b) pore size distributions by adsorption branches of *hs*CN, 0.34Ru-*hs*CN and 0.34Ru-*hs*CN-*imp*.

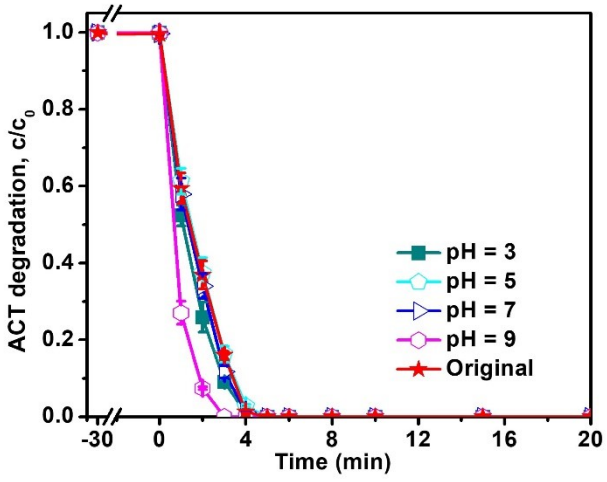

Figure S4. The effect of initial pH value on the adsorption and degradation of ACT by 0.34Ru-*hs*CN/PMS. ([Catalyst]$_0$ = 0.2 g·L^{-1}, [PMS]$_0$ = 2.0 g·L^{-1}, [T] = 25 °C, [ACT]$_0$ = 20 mg·L^{-1}).

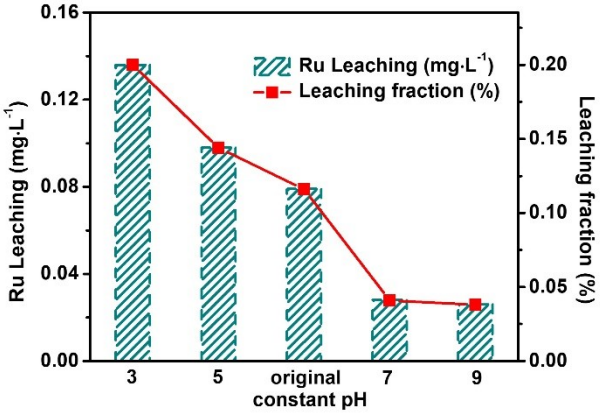

Figure S5. Ru leaching at different constant pH during the adsorption and degradation of ACT by 0.34Ru-*hs*CN/PMS. ([Catalyst]$_0$ = 0.2 g·L^{-1}, [PMS]$_0$ = 2.0 g·L^{-1}, [T] = 25 °C, [ACT]$_0$ = 20 mg·L^{-1}).

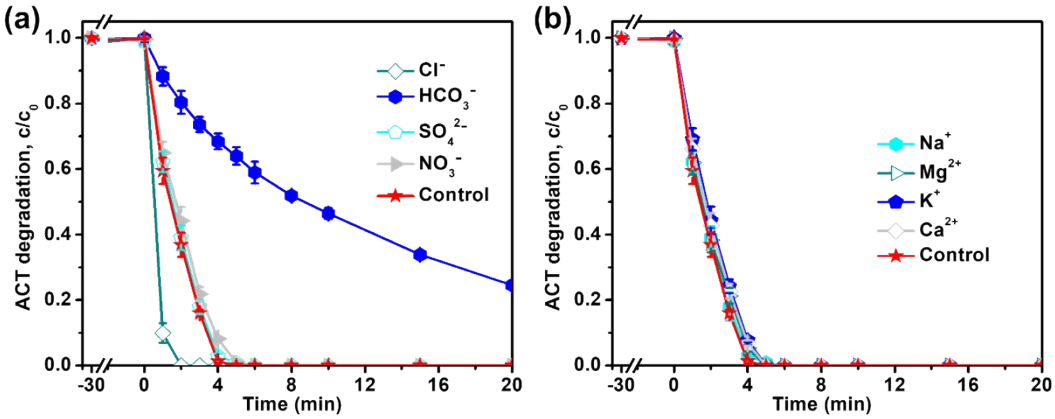

Figure S6. Effects of reaction parameters on the ACT degradation for 0.34Ru-*hs*CN/PMS: (a) inorganic anions, (b) inorganic cations. ([Catalyst]$_0$ = 0.2 g·L^{-1}, [PMS]$_0$ = 2.0 g·L^{-1}, [T] = 25 ° C, [ACT]$_0$ = 20 mg·L^{-1}, [NaCl]$_0$ = 5 mM, [$NaHCO_3$]$_0$ = 5 mM, [Na_2SO_4]$_0$ =5 mM, and [$NaNO_3$]$_0$ = 5 mM, [$MgSO_4$]$_0$ = 5 mM, [K_2SO_4]$_0$ = 2.5 mM, and [$CaSO_4$]$_0$ =5 mM).

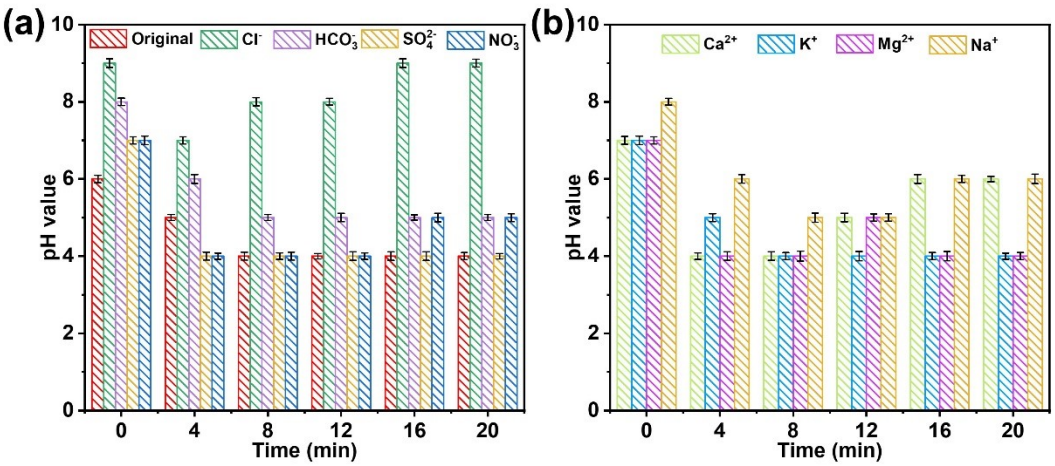

Figure S7. The changes of pH values after ion addition on the ACT degradation for 0.34Ru-*hs*CN/PMS: (a) inorganic anions and (b) cations. ([Catalyst]$_0$ = 0.2 g·L^{-1}, [PMS]$_0$ = 2.0 g·L^{-1}, [T] = 25 ℃, [ACT]$_0$ = 20 mg·L^{-1}, [NaCl]$_0$ = 5 mM, [$NaHCO_3$]$_0$ = 5 mM, [Na_2SO_4]$_0$ =5 mM, and [$NaNO_3$]$_0$ = 5 mM, [$MgSO_4$]$_0$ = 5 mM, [K_2SO_4]$_0$ = 2.5 mM, and [$CaSO_4$]$_0$ =5 mM).

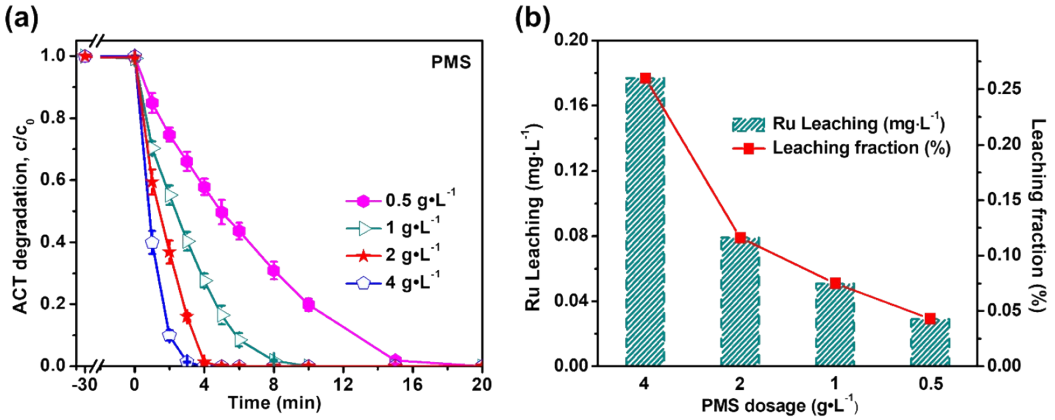

Figure S8. (a) The effect of PMS dosage on the adsorption and degradation of ACT by 0.34Ru-*hs*CN/PMS system, (b) Leaching of Ru with different PMS dosage. ([Catalyst]$_0$ = 0.2 g·L^{-1}, [T] = 25 ^{o}C, and [ACT]$_0$ = 20 mg·L^{-1}).

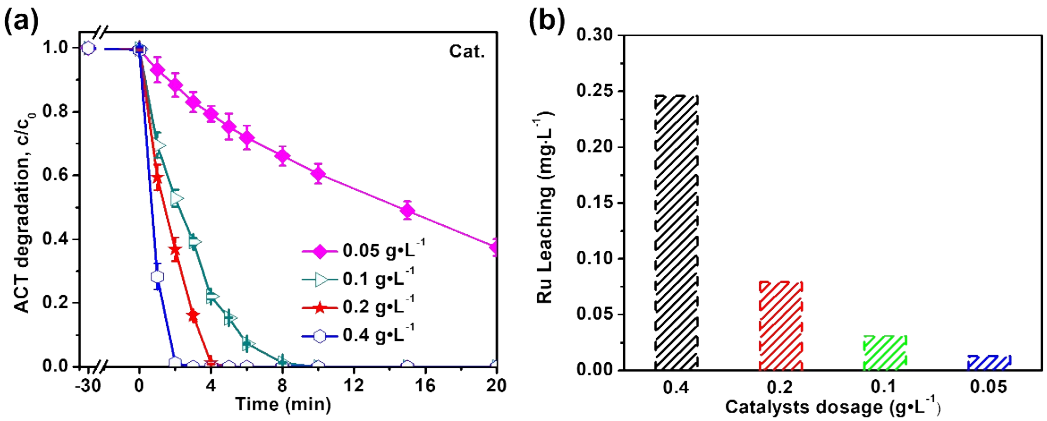

Figure S9. (a) The influence of catalyst dosage on the adsorption and degradation of ACT by 0.34Ru-*hs*CN/PMS system, (b) Leaching of Ru with different catalyst dosage. ($[PMS]_0$ = 2.0 g·L^{-1}, [T] = 25 °C, and $[ACT]_0$ = 20 mg·L^{-1})

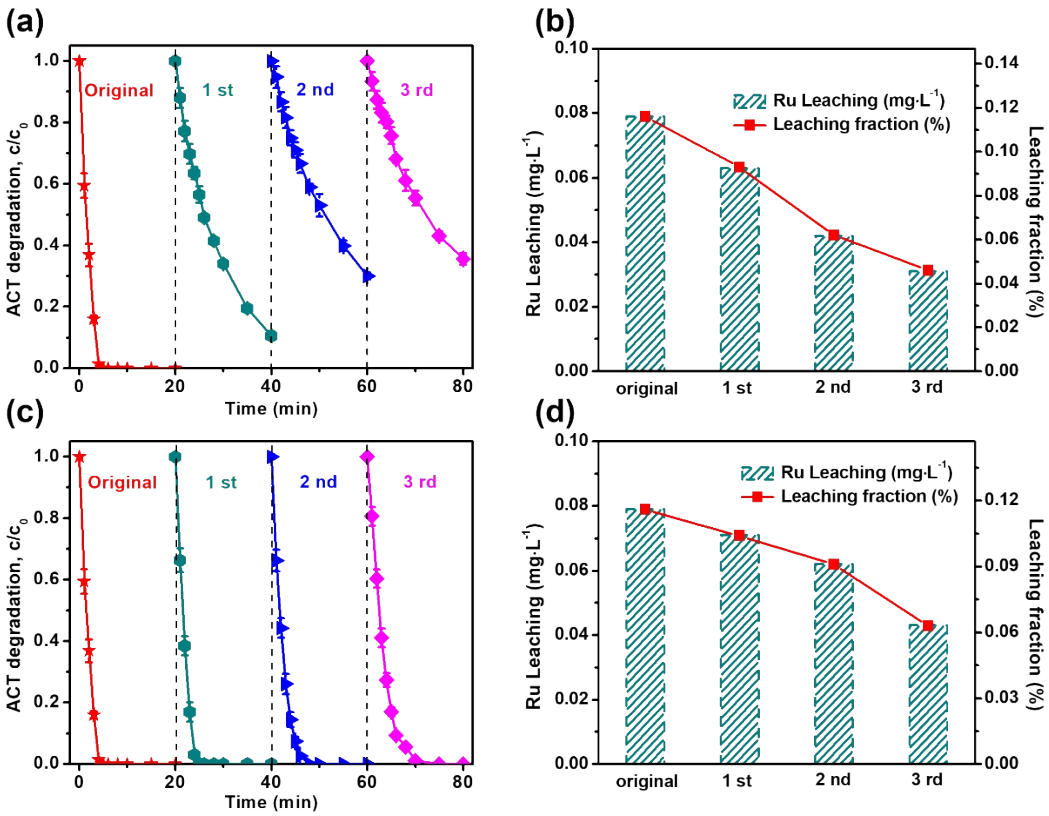

Figure S10. (a) Three repeated cycling degradation of ACT by 0.34Ru-*hs*CN/PMS system, (b) regeneration cycles of 0.34Ru-*hs*CN/PMS for ACT degradation reaction. ([Catalyst]$_0$ = 0.2 g·L^{-1}, [PMS]$_0$ = 2.0 g·L^{-1}, [T] = 25 °C, and [ACT]$_0$ = 20 mg·L^{-1}).

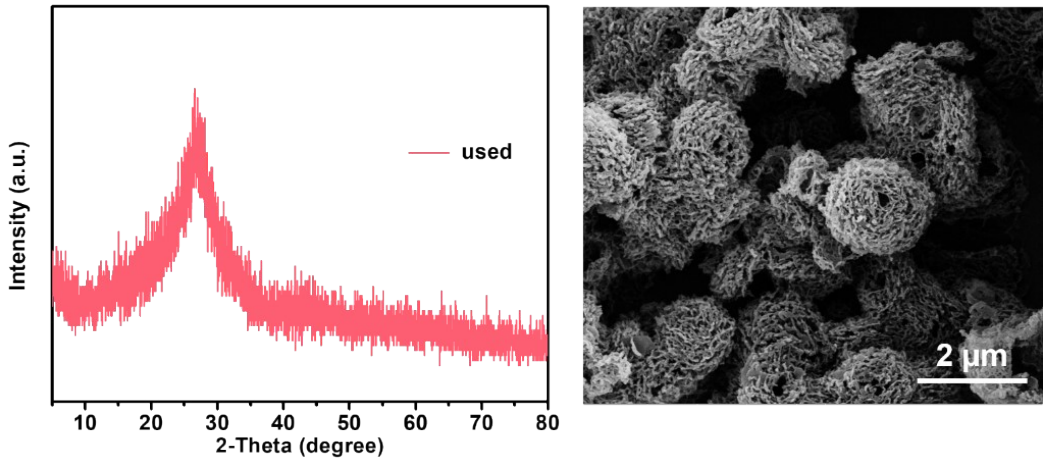

Figure S11. (a) XRD and (b) SEM image of used 0.34Ru-*hs*CN.

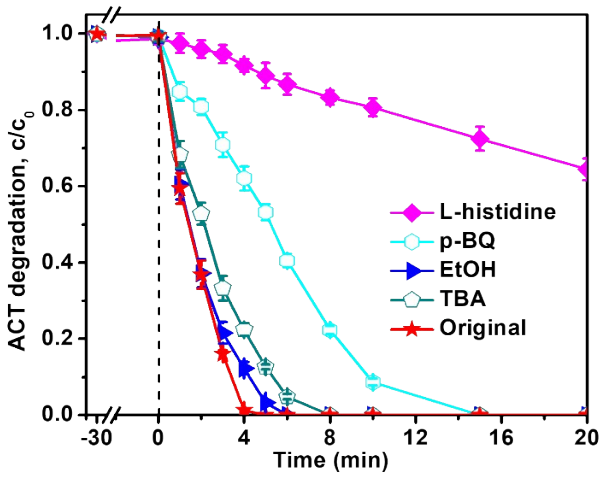

Figure S12. Effect of different quenching agents on ACT degradation for 0.34Ru-hsCN/PMS system. ($[Catalyst]_0$ = 0.2 $g \cdot L^{-1}$, $[PMS]_0$ = 2.0 $g \cdot L^{-1}$, [T] = 25 ° C, $[ACT]_0$ = 20 $mg \cdot L^{-1}$, $[EtOH]_0$ = 0.2 M, $[TBA]_0$ = 0.2 M, $[L\text{-histidine}]_0$ =5 mM, and $[p\text{-BQ}]_0$ = 5 mM).

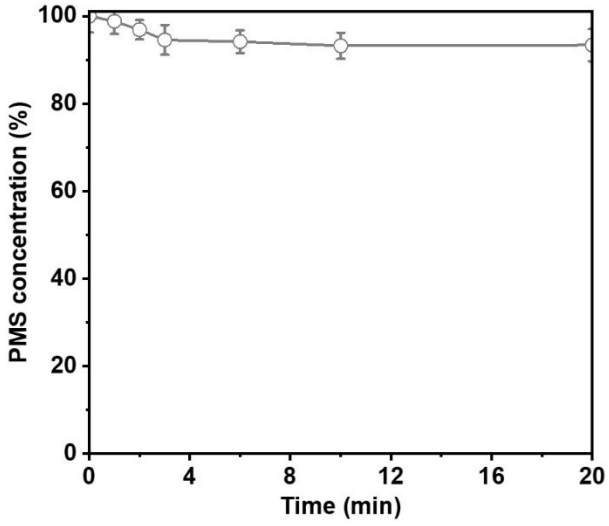

Figure S13. Variation of PMS concentration in the reactions with L-histidine. ($[PMS]_0$=2.0 $g \cdot L^{-1}$, $[L\text{-histidine}]_0$=5 mM, [T]=25 °C).

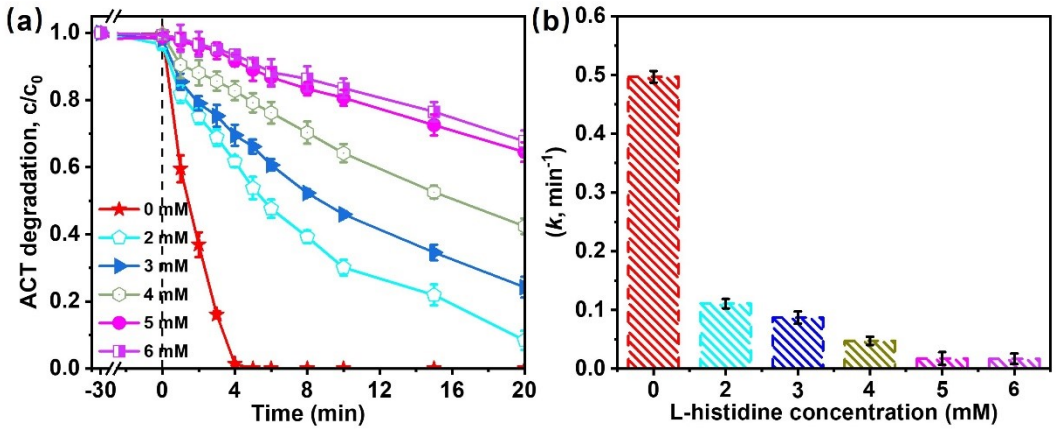

Figure S14. (a) Influences of L-histidine concentration, (b) changes of *k* with different amount of L-histidine on ACT degradation for 0.34Ru-*hs*CN/PMS system. ($[Catalyst]_0$ = 0.2 $g \cdot L^{-1}$, $[PMS]_0$ = 2.0 $g \cdot L^{-1}$, [T] = 25 °C, and $[ACT]_0$ = 20 $mg \cdot L^{-1}$)

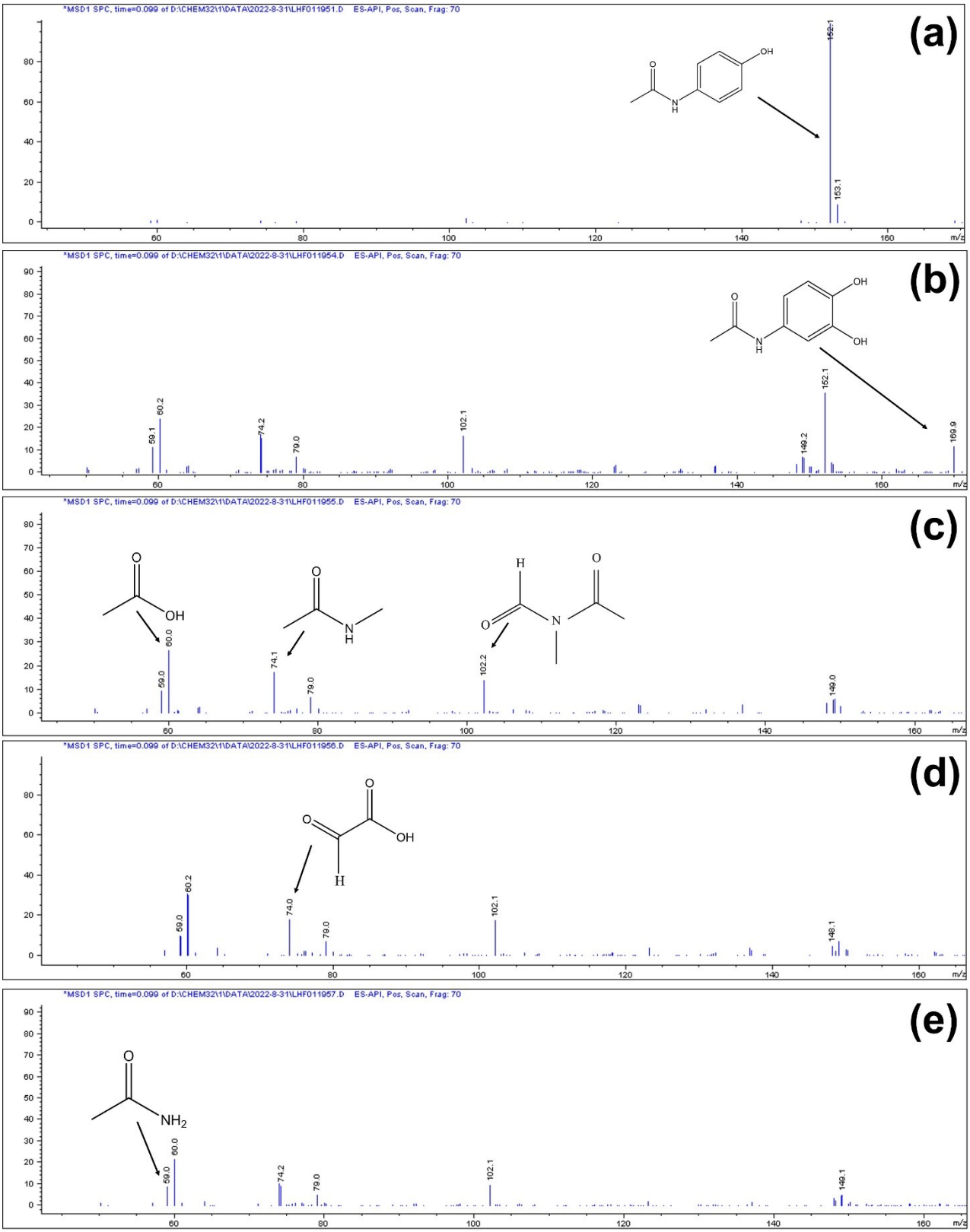

Figure S15. LC-MS spectra and proposed structure of intermediates during ACT degradation for the 0.34Ru-*hs*CN/PMS system after (a) 0 min, (b) 2 min, (c) 5 min, (d) 10 min, and (e) 20 min. ($[Catalyst]_0$ = 0.2 g·L^{-1}, $[PMS]_0$ = 2.0 g·L^{-1}, [T] = 25 °C, and $[ACT]_0$ = 20 mg·L^{-1}).

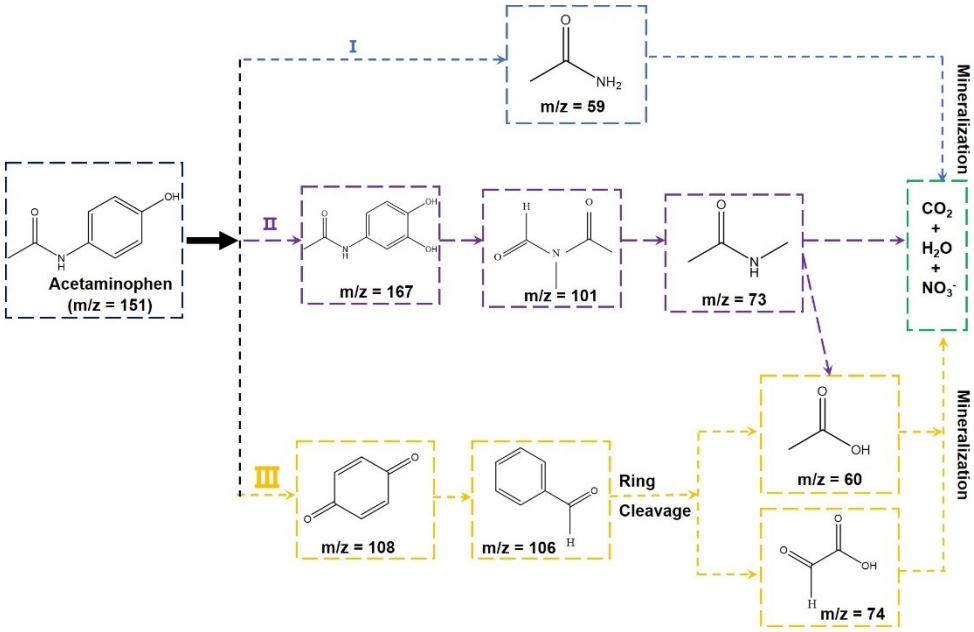

Figure S16. Proposed degradation pathway during ACT degradation for the 0.34Ru-*hs*CN/PMS system. ($[Catalyst]_0$ = 0.2 g·L^{-1}, $[PMS]_0$ = 2.0 g·L^{-1}, [T] = 25 °C, and $[ACT]_0$ = 20 mg·L^{-1}).

Table S1. BET surface areas and pore volumes of the prepared samples.

Catalyst	S_{BET} (m^2/g)	Pore volume (cm^3/g)
*hs*CN	96	0.351
0.34Ru-*hs*CN	119	0.464
0.34Ru-*hs*CN-*imp*	58	0.167

Table S2. ACT degradation in various catalytic systems.

Catalyst	k_{app} (min^{-1})	R^2	Removal (%)
PMS	0.0019	0.998	1.9% (20 min)
*hs*CN + PMS	0.0054	0.973	3.0% (20 min)
0.34Ru-*hs*CN + PMS	0.497	0.999	100% (5 min)
Leaching Ru ions + PMS	0.041	0.970	21.0% (20 min)
0.34Ru-*hs*CN-*imp* + PMS	0.027	0.963	34.4% (20 min)
0.34Ru-*hs*CN + Cl^- + PMS	2.337	0.999	100% (2 min)

Table S3. The catalytic performances of various reported materials on ACT degradation

Catalyst	Operating conditions				Activity	Rate constant (k, min^{-1})	Ref.
	Temp.	$[ACT]_0$	$[Catalyst]_0$	PMS			
0.34Ru-*hs*CN	25 °C	20 $mg·L^{-1}$	0.2 $g·L^{-1}$	6.5 mM	100% 5 min	0.497	this work
Fe-S_1@NC	25 °C	20 $mg·L^{-1}$	2 $mg·L^{-1}$	0.5 mM	100% 7 min	0.7290	1
0.1%SA-Co CNP	25 °C	20 $mg·L^{-1}$	0.2 $g·L^{-1}$	1.625mM	92% 10 min	0.51	2
0.50-Mn-CN	25 °C	20 $mg·L^{-1}$	0.2 $g·L^{-1}$	2.6 mM	100% 15 min	0.32	3
5% $Co(OH)_2$/g-C_3N_4	25 °C	3.02 $mg·L^{-1}$	0.5 $g·L^{-1}$	5 mM	92% 30 min	0.193	4
0.5-Mn_3O_4-CN	25 °C	20 $mg·L^{-1}$	0.1 $g·L^{-1}$	2.5 mM	100% 60 min	0.085	5
CF/MCN	25 °C	15 $mg·L^{-1}$	40 $mg·L^{-1}$	1.5 mM	92% 25 min	0.1023	6
Fe-N@C-900	25 °C	10 $mg·L^{-1}$	0.1 $g·L^{-1}$	0.5 mM	100% 15 min	0.2472	7
Co_3O_4@NSC-900	25 °C	10 $mg·L^{-1}$	0.1 $g·L^{-1}$	0.5 mM	100% 45 min	0.162	8
Fe/TNTs	25 °C	1.5 $mg·L^{-1}$	0.1 $g·L^{-1}$	0.1 mM	95.2% 30 min	0.154	9
Mn_2O_3-Fe_2O_3	25 °C	15 $mg·L^{-1}$	0.05 $g·L^{-1}$	0.5 mM	100% 15 min	0.33	10
S-MgO	25 °C	50 $mg·L^{-1}$	1 $g·L^{-1}$	3.25 mM	100% 30 min	0.314	11
NS-CMK-3	25 °C	50 $mg·L^{-1}$	0.1$g·L^{-1}$	0.5 mM	100% 30 min	0.24	12
NOE-PC-300	25 °C	20 $mg·L^{-1}$	0.2 $g·L^{-1}$	1 mM	100% 20 min	–	13
FeOCl	25 °C	1.5 $mg·L^{-1}$	0.2 $g·L^{-1}$	2 mM	100% 20 min	0.3	14
$CoFe_2O_4$	25 °C	40 $mg·L^{-1}$	0.2 $g·L^{-1}$	0.2 mM	100% 120 min	0.053	15
$MnFe_2O_4$	25 °C	40 $mg·L^{-1}$	0.2 $g·L^{-1}$	0.2 mM	100% 30 min	0.121	15
$Na_2B_4O_7$	75 °C	1.5 $mg·L^{-1}$	10 mM	1.5 mM	100% 15 min	0.298	16
Fe_3O_4	25 °C	10 $mg·L^{-1}$	0.8 $g·L^{-1}$	0.2 mM	74.7% 120 min	0.012	17
Fe^{2+} + MoS_2	25 °C	20 $mg·L^{-1}$	$FeSO_4·7H_2O$=0.02 $g·L^{-1}$ MoS_2=01 $g·L^{-1}$	0.5 mM	94.5% 200 min	0.1099	18

Table S4. The reaction rate constants between scavengers and targeted radicals

Scavenger	Targeted radical	Rate constant (k, $M^{-1}\cdot s^{-1}$)
EtOH	$SO_4^{\bullet -}$ / $^{\bullet}OH$	1.6×10^7 / 1.9×10^9
TBA	$^{\bullet}OH$	$(3.8 \sim 7.6) \times 10^8$
p-BQ	$O_2^{\bullet -}$	$(0.9 \sim 1.0) \times 10^9$
L-histidine	$^1O_2$	3.2×10^7

References

1 Y. Chen, Q. Liang, Y. Deng, Y. Bin, T. Wang and H. Luo, Peroxymonosulfate activation by concave porous S/N co-doped carbon: Singlet oxygen-dominated non-radical efficient oxidation of organics, *J. Environ. Chem. Eng.*, 2022, **10**, 107933, doi: 10.1016/j.jece.2022.107933.

2 G. Liao, X. Qing, P. Xu, L. Li, P. Lu, W. Chen and D. Xia, Synthesis of single atom cobalt dispersed on 2D carbon nanoplate and degradation of acetaminophen by peroxymonosulfate activation, *Chem. Eng. J.*, 2022, **427**, 132027, doi: 10.1016/j.cej.2021.132027.

3 J. Fan, H. Qin and S. Jiang, Mn-doped g-C_3N_4 composite to activate peroxymonosulfate for acetaminophen degradation: The role of superoxide anion and singlet oxygen, *Chem. Eng. J.*, 2019, **359**, 723-732, doi: 10.1016/j.cej.2018.11.165.

4 L. Wang, X. Li, H. Chen, Y. Liang, Z. Xu, J. Liu, W. Liu and J. Qi, Optimizing co site electron structure by construction of heterogeneous interface for efficient sulfite activation on paracetamol removal, *J. Environ. Chem. Eng.*, 2022, **10**, 108660, doi: 10.1016/j.jece.2022.108660.

5 J. Fan, Q. Wang, W. Yan, J. Chen, X. Zhou and H. Xie, Mn_3O_4-g-C_3N_4 composite to activate peroxymonosulfate for organic pollutants degradation: Electron transfer and structure-dependence, *J. Hazard. Mater.*, 2022, **434**, 128818, doi: 10.1016/j.jhazmat.2022.128818.

6 A. Hassani, P. Eghbali, B. Kakavandi, K.-Y. A. Lin and F. Ghanbari, Acetaminophen removal from aqueous solutions through peroxymonosulfate activation by $CoFe_2O_4$/mpg-C_3N_4 nanocomposite: Insight into the performance and degradation kinetics, *Environ. Technol. Inno.*, 2020, **20**, 101127, doi: 10.1016/j.eti.2020.101127.

7 C. Chen, T. Ma, Y. Shang, B. Gao, B. Jin, H. Dan, Q. Li, Q. Yue, Y. Li, Y. Wang and X. Xu, In-situ pyrolysis of enteromorpha as carbocatalyst for catalytic removal of organic contaminants: Considering the intrinsic N/Fe in enteromorpha and non-radical reaction, *Appl. Catal., B*, 2019, **250**, 382-395, doi: 10.1016/j.apcatb.2019.03.048.

8 L. Peng, Y. Shang, B. Gao and X. Xu, Co_3O_4 anchored in N, S heteroatom co-doped porous carbons for degradation of organic contaminant: Role of pyridinic N-Co binding and high tolerance of chloride, *Appl. Catal., B*, 2021, **282**, 119484, doi: 10.1016/j.apcatb.2020.119484.

9 J. Ma, L. Chen, Y. Liu, T. Xu, H. Ji, J. Duan, F. Sun and W. Liu, Oxygen defective titanate nanotubes induced by iron deposition for enhanced peroxymonosulfate activation and acetaminophen degradation: Mechanisms, water chemistry effects, and theoretical calculation, *J. Hazard. Mater.*, 2021, **418**, 126180, doi: 10.1016/j.jhazmat.2021.126180.

10 W. Tan, W. Ren, C. Wang, Y. Fan, B. Deng, H. Lin and H. Zhang, Peroxymonosulfate activated with waste

battery-based Mn-Fe oxides for pollutant removal: Electron transfer mechanism, selective oxidation and LFER analysis, *Chem. Eng. J.*, 2020, **394**, 124864, doi: 10.1016/j.cej.2020.124864.

11 F. Fanaei, G. Moussavi, V. Srivastava and M. Sillanpää, The enhanced catalytic potential of sulfur-doped MgO (S-MgO) nanoparticles in activation of peroxysulfates for advanced oxidation of acetaminophen, *Chem. Eng. J.*, 2019, **371**, 404-413, doi: 10.1016/j.cej.2019.04.007.

12 P. Sun, H. Liu, M. Feng, X. Zhang, Y. Fang, Z. Zhai and V. K. Sharma, Dual nonradical degradation of acetaminophen by peroxymonosulfate activation with highly reusable and efficient N/S co-doped ordered mesoporous carbon, *Sep. Purif. Technol.*, 2021, **268**, 118697, doi: 10.1016/j.seppur.2021.118697.

13 M. Xu, Q. Zhang, Z. Zhu, Y. Xue, T. Zhang and J. Hong, Chemical etching to regulation oxygen vacancies on Mn-Fe PBA for highly efficient degradation of bisphenol A and acetaminophen, *J. Cleaner Prod.*, 2022, **377**, 134258, doi: 10.1016/j.jclepro.2022.134258.

14 C. Tan, Q. Xu, T. Sheng, X. Cui, Z. Wu, H. Gao and H. Li, Reactive oxygen species generation in FeOCl nanosheets activated peroxymonosulfate system: Radicals and non-radical pathways, *J. Hazard. Mater.*, 2020, **398**, 123084, doi: 10.1016/j.jhazmat.2020.123084.

15 C. Tan, N. Gao, D. Fu, J. Deng and L. Deng, Efficient degradation of paracetamol with nanoscaled magnetic $CoFe_2O_4$ and $MnFe_2O_4$ as a heterogeneous catalyst of peroxymonosulfate, *Sep. Purif. Technol.*, 2017, **175**, 47-57, doi: 10.1016/j.seppur.2016.11.016.

16 J. Li, J. Zou, S. Zhang, H. Cai, Y. Huang, J. Lin, Q. Li, B. Yuan and J. Ma, Sodium tetraborate simultaneously enhances the degradation of acetaminophen and reduces the formation potential of chlorinated by-products with heat-activated peroxymonosulfate oxidation, *Water Res.*, 2022, **224**, 119095, doi: 10.1016/j.watres.2022.119095.

17 C. Tan, N. Gao, Y. Deng, J. Deng, S. Zhou, J. Li and X. Xin, Radical induced degradation of acetaminophen with Fe_3O_4 magnetic nanoparticles as heterogeneous activator of peroxymonosulfate, *J. Hazard. Mater.*, 2014, **276**, 452-460, doi: 10.1016/j.jhazmat.2014.05.068.

18 Y. Zhang, J. Niu and J. Xu, Fe(II)-promoted activation of peroxymonosulfate by molybdenum disulfide for effective degradation of acetaminophen, *Chem. Eng. J.*, 2020, **381**, 122718, doi: 10.1016/j.cej.2019.122718.